

Research Article

In Situ Stress Effects on Smooth Blasting: Model Test and Analysis

Renshu Yang,^{1,2,3} Shizheng Fang¹,,¹ Aiyun Yang,¹ Huanzhen Xie,¹ and Liyun Yang¹

¹School of Mechanics and Civil Engineering, China University of Mining and Technology, Beijing 100083, China

²State Key Laboratory for Geo-mechanics and Deep Underground Engineering, China University of Mining and Technology, Beijing 100083, China

³Beijing Key Laboratory of Urban Underground Space Engineering, School of Civil and Resource Engineering, University of Science and Technology Beijing, Beijing 100083, China

Correspondence should be addressed to Liyun Yang; yangly@cumtb.edu.cn

Received 25 August 2019; Revised 15 November 2019; Accepted 25 November 2019; Published 7 January 2020

Academic Editor: Isabelle Sochet

Copyright © 2020 Renshu Yang et al. This is an open access article distributed under the Creative Commons Attribution License, which permits unrestricted use, distribution, and reproduction in any medium, provided the original work is properly cited.

Most of the roadway excavation is completed by the drilling and blasting method. With the increase of buried depth, the existence of ground stress will generate a significant impact on the rock blasting, especially on the smooth blasting. In this study, self-made homogeneous similar materials and digital image correlation methods were used to determine influence of ground stress on the smooth blasting under uniform explosive charge parameters and various in situ stress conditions. The results show that the crack outline after blasting changes from zigzag to straight in shape, and multifractal calculation results of the rupture section between blastholes show that the fracture surface becomes flatter as ground stress increases, which is conducive to roadway formation. The strain and equivalent strain rate obviously decrease as the distance between the blasthole and measuring points increases. The same trend occurs as the confining pressure goes up. Meanwhile, a postexplosion acoustic wave test indicates that confining pressure inhibits damage of the retained rock, which is consistent with strain and equivalent strain rate results. Finally, we discussed the crack propagation mechanism of rock in smooth blasting.

1. Introduction

Drilling-blasting techniques are often used in coal mining, tunnel excavation, and other projects [1–4]. The geological conditions are more complicated at greater depths which have grown more common in recent years. The influence of initial in situ stress on blasting becomes more significant as ground stress increases, for example. The blasting effect is strengthened or weakened by stress, and the deep blasting rock failure mechanism is very complex. Geological issues can cause serious safety problems in coal mining operations. Blasting engineers must ensure reasonable and effective crushing of the rock mass throughout the excavation process. It is also necessary to minimize damage to the rock masses outside the excavation profile as much as possible. Smooth blasting is conducted for this purpose [5].

There are numerous research studies about blasting issues under an initial stress field [6–9]. Kutter and Fairhurst [10] explored the effects of explosion stress waves and explosive

gas on crack propagation to find that blast-induced cracks extend toward the direction of the maximum principal stress in the static stress field. Rossmann et al. [11] studied the dynamic evolution of three-dimensional cracks under a combination of blasting and uniaxial stress; they gathered valuable physical and mechanical information regarding crack propagation under blasting loading which can be utilized for numerical simulations. Liu et al. [12] conducted a photoelastic experiment to observe the propagation mechanism of the explosion stress wave under an initial stress condition. Liu and Xu [13] numerically simulated a rock blasting process to find that the influence of ground stress is related to the distance of the explosive charge. The stress wave dominates the region near the explosion charge over the ground stress. In the far-explosive area, the presence of ground stress significantly alters the stress wave propagation.

There have been some valuable contributions to the smooth blasting. Lu et al. [14], for example, considered the effect of original stress field on the construction of an

2.2. Explosive Charge and Blasting Parameter Design. The explosive used in this study is made of modified gunpowder (MGP). The outer covering of the charge is made of polyethylene. The height of the explosive L_0 is 30 mm, the length of the charge L_1 is 40 mm, and the diameter of the charge D_1 is 5 mm. The explosive charge parameters are shown in Table 1. A detonation probe is embedded in the charge, generating a high-pressure discharge to detonate the explosive.

Three blastholes with same geometric dimensions are placed on one side of the specimen, each with diameter D_2 and depth L_2 of 7 mm and 60 mm, respectively. The distance between blastholes L_3 is 40 mm, and the uncoupling coefficient is 1.4. The charge is placed at the bottom of the blasthole, and the detonation mode is indirect. Sand and glue are used for sealing. The layout of the blastholes and explosive charge are shown in Figure 4.

2.3. Test Principle and Equipment. DIC technique is a noncontact optical method for full-field strain measurement. The speckles on the sample surface move as the specimen deforms. The principle of DIC algorithm is to match the speckle image before and after object deformation to reveal the displacement and strain of the specimen [20–22]. It is operated as follows: the gray matrix of the digital speckle image is calculated before and after the specimen surface deformation to track the point spatial deformation, and then the surface displacement and strain information of the specimen can be obtained. The basic principle is shown in Figure 5.

As shown in Figure 5, the coordinate relationship of the subarea center $P(x_0, y_0)$ before and after the deformation is calculated as follows:

$$\begin{aligned} x'_0 &= x_0 + u, \\ y'_0 &= y_0 + v, \end{aligned} \quad (1)$$

where u and v are the vertical and horizontal displacement, respectively, and (x'_0, y'_0) is the position of point P after deformation. Based on the theory of continuum mechanics, the displacement of a point can be expressed by the displacement and increment of its adjacent point. So, the displacement (u_Q, v_Q) of the $Q(x, y)$, which was randomly selected in the reference subarea, can be expressed as follows:

$$\begin{aligned} u_Q &= u + \frac{\partial u}{\partial x} \Delta x + \frac{\partial u}{\partial y} \Delta y, \\ v_Q &= v + \frac{\partial v}{\partial x} \Delta x + \frac{\partial v}{\partial y} \Delta y, \end{aligned} \quad (2)$$

where Δx and Δy are the horizontal and the vertical deformation increment, respectively. The area of interest (AOI) in this test is a partial area of the preserved rock mass, as shown in Figure 6. The surface of the specimen was cleaned to ensure it was sufficiently flat, and a spattering method was used to make speckles on the surface of the specimen, and then black speckles were printed onto it in

randomly distributed sizes. The average grayscale gradient satisfies the recommended value [23, 24].

The high-speed DIC (HS-DIC) method test system [25] is mainly composed of a program-controlled multichannel pulse igniter, a signal source, a flash controller, a high-speed camera, a camera status indicator, and a computer. A schematic diagram of the setup is provided in Figure 7. A high-speed camera (Kirana) was selected because of its unique μ CMOS sensor, 100 ns high-speed global electronic shutter, and image resolution fixed at 924×768 pixels. The image resolution does not decrease as the acquisition frequency increases. This effectively guarantees the feasibility of the camera's full-field shooting and subsequent full-field deformation analysis of the specimen.

This test mainly focused on the influence of ground stress on smooth blasting. Three sets of schemes were designed for the test and recorded as G1, G2, and G3. The blasting parameters were completely consistent and the vertical static load was set to 0, 1, or 2 MPa successively. After the test, the fracture morphology, strain evolution, and damage distribution characteristics of each specimen under different initial stress fields were analyzed and compared. The results are described in detail below.

3. Test Results and Analysis

3.1. Analysis of Specimen Fracture Profile Modes. Figure 8 shows the specimen crack profile after testing and a schematic view extracted from the crack profile. As shown in Figures 8, when the confining pressure is 0 MPa, the shape of the edge of the crack is irregularly jagged; when the confining pressure is 1 MPa, the crack exhibits an irregular arc shape but the curvature is small. When the pressure rises to 2 MPa, the shape of the crack is regular. It appears that as the pressure of the surrounding rock increased, the crack gradually moved from an irregular zigzag shape to a regular straight line. The existence of confining pressure made the rupture more regular [10].

To quantitatively analyze the variation characteristics of the fracture surface after smooth blasting, the fracture surface between the blastholes was extracted, as shown in Figure 9. The multifractal spectrum theory [26] was used to analyze the roughness of the fracture surface between the blastholes. The multifractal spectrum can be expressed as follows:

$$f(\alpha) = \frac{\lg[N(\alpha)]}{\lg[b(\delta)]}, \quad (3)$$

where $f(\alpha)$ is the multifractal dimension, α is a scaling index singular value, $N(\alpha)$ is the number of corresponding boxes, δ is the spacing of the ruler to measure the fractal subset, and $b(\delta)$ is the size of the covering box. Figure 10 shows the multifractal curve of each fracture surface under different confining pressures.

The multifractal spectrum width $\Delta\alpha = \alpha_{\max} - \alpha_{\min}$ reflects the fluctuation amplitude of the surface roughness of the fracture surface as well as the degree of its unevenness. A larger $\Delta\alpha$ value indicates a rougher fracture surface between the blastholes after blasting. A smaller $\Delta\alpha$ indicates more

TABLE 1: Explosive charge parameters.

Type of explosive	Detonation velocity v , (m/s)	Charge weight (mg)	Explosive charge diameter D_1 (mm)	Explosive charge height L_1 (mm)	Explosive height L_0 (mm)	Explosive density ρ (g/cm ³)
MGP	400	250	5	40	30	0.523

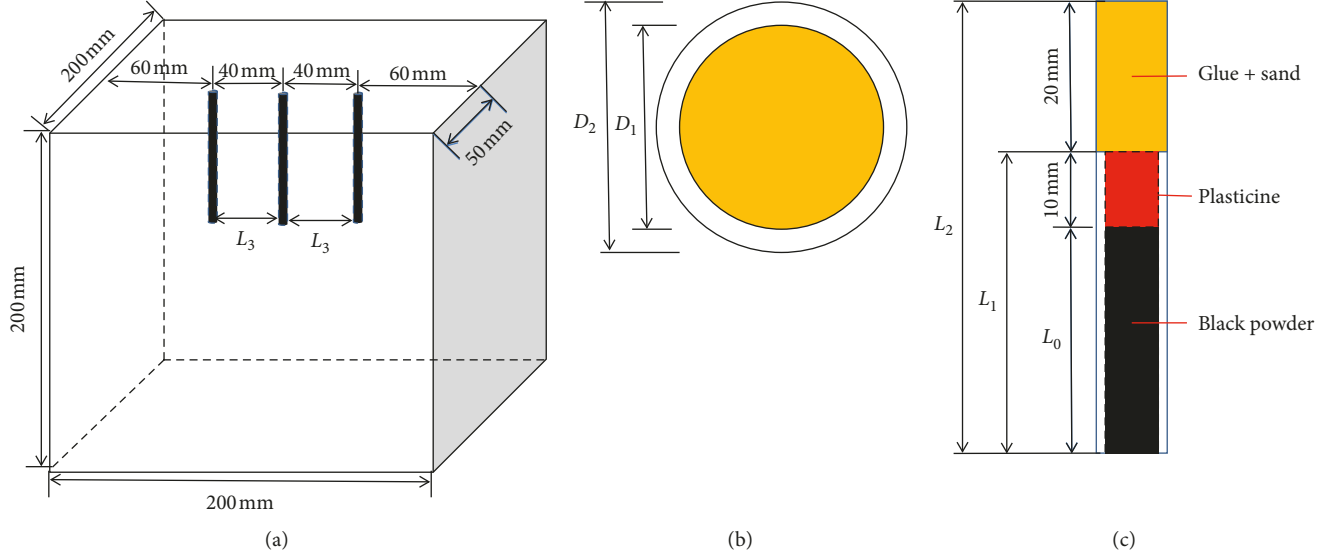


FIGURE 4: Schematic diagram of blastholes and explosive charge. (a) Global view. (b) Top view of blasthole. (c) Parameters of explosive charge.

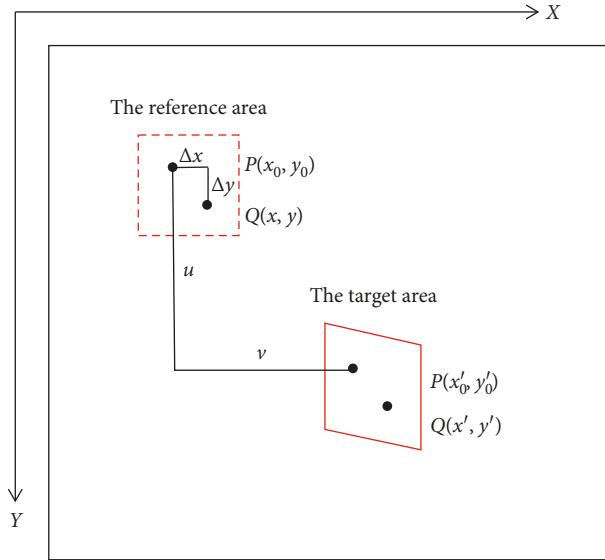


FIGURE 5: DIC basic principles.

similar crack surface undulations and a more uniform crack distribution on the surface.

Table 2 shows the multifractal spectrum calculation parameters. I_{AS} is an asymmetry index, and its absolute value characterizes the degree of unevenness on the crack surface and the distribution tendency of microcracks to change from uneven to uniform. $I_{AS} = (L - R)/(L + R)$, where L and R are the horizontal distance from the left

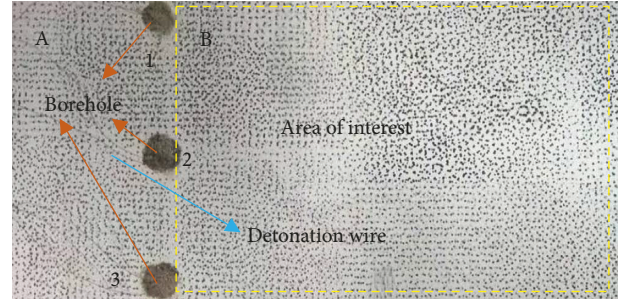


FIGURE 6: Image of specimen with speckles.

endpoint and the right endpoint to the maximum point in the multifractal spectrum curve, respectively. The corresponding dimensional difference Δf ($\Delta f = f(\alpha_{\min}) - f(\alpha_{\max})$) reflects the variations in the maximum fluctuation amplitude and minimum fluctuation amplitude of the fracture surface. The multifractal parameter width $\Delta\alpha$, the dimension difference Δf , and the maximum value f_{\max} of the blasting fracture surface all decrease as confining pressure increases, which indicates that the microcrack distribution of the fracture was wider under nonconfining pressure and the blasting destructive effect was stronger. The absolute value of the multifractal spectrum I_{AS} decreases as confining pressure increases, which reflects the tendency of the unevenness of the surrounding rock wall and the distribution of the cracks from uneven to regular after smooth blasting.

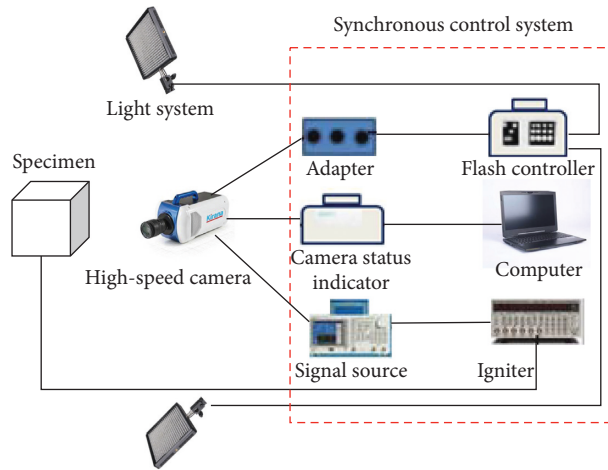


FIGURE 7: Experimental system.

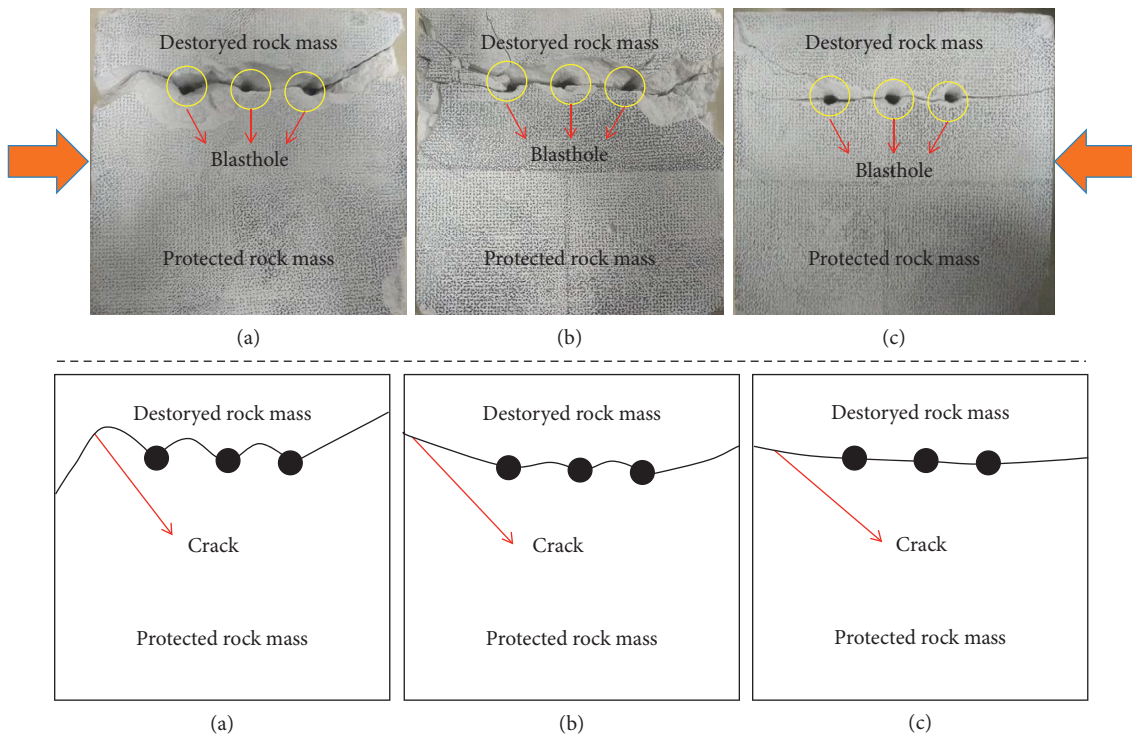


FIGURE 8: Raw image and sketch of blasting crack outline. (a) 0 MPa, (b) 1 MPa, and (c) 2 MPa.

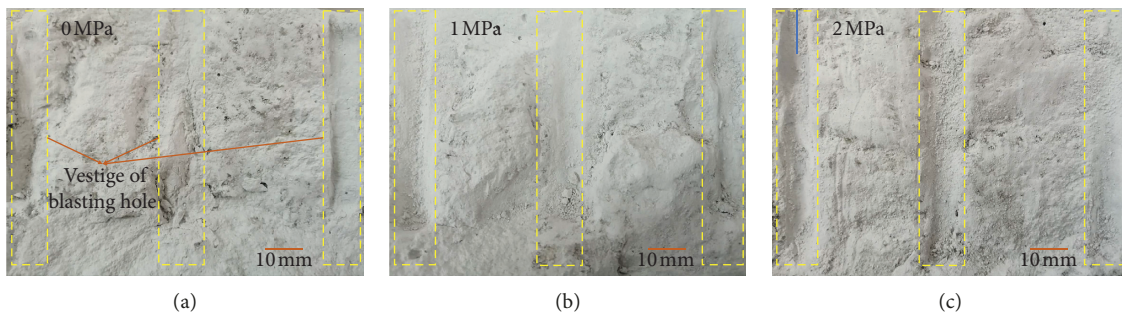


FIGURE 9: Cross section between blastholes after blasting.

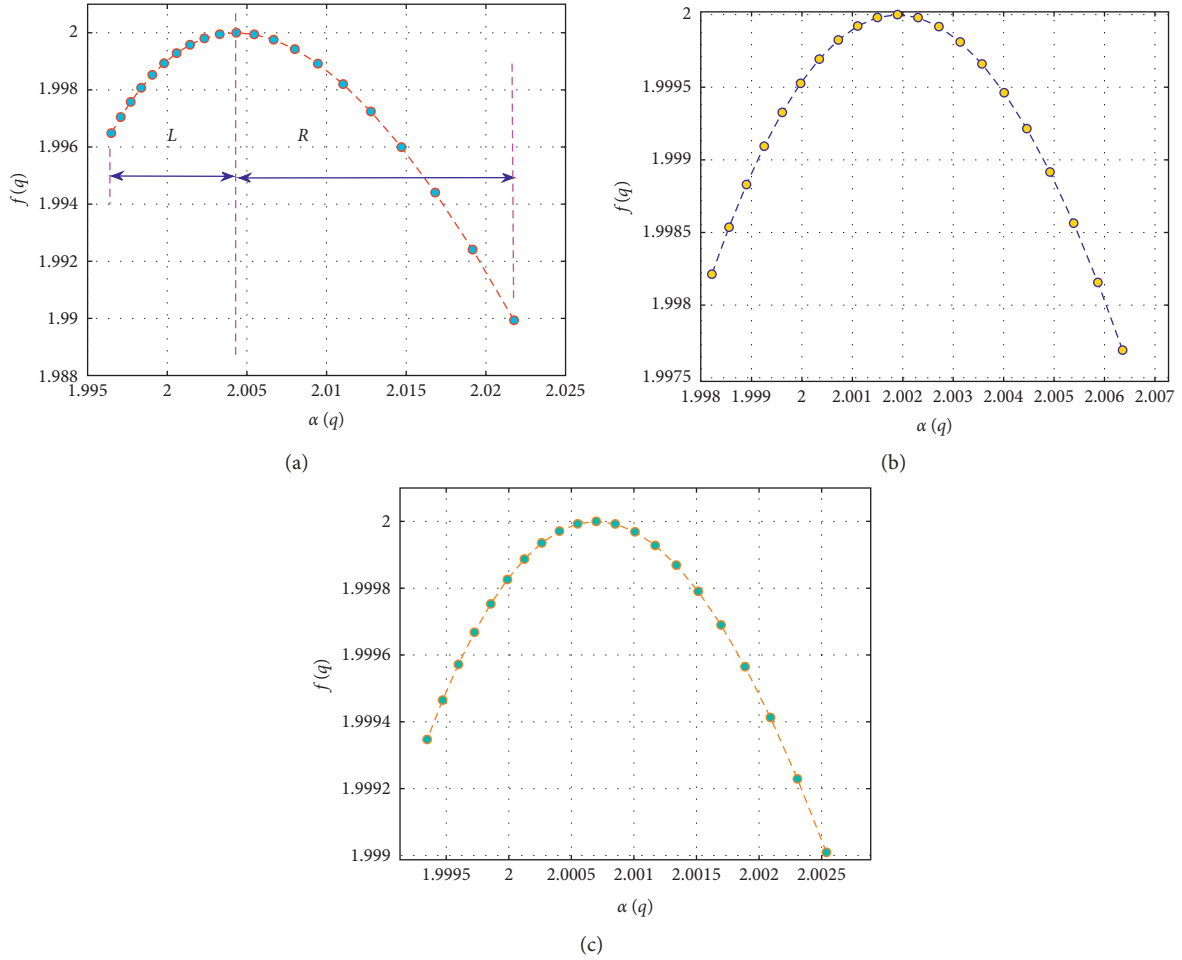


FIGURE 10: Multifractal curves of blast-induced fracture surface. (a) 0 MPa. (b) 1 MPa. (c) 2 MPa.

TABLE 2: Multifractal parameters of blast-induced crack surface under different confining pressures.

Confining pressure (MPa)	$\Delta\alpha$	Δf	f_{\max}	I_{AS}
0	0.0261	0.0122	2.0017	-0.4176
1	0.0101	0.0029	2.0006	-0.3069
2	0.0032	0.0011	2.0002	-0.1875

3.2. Strain and Equivalent Strain Rate Attenuation of Retained Rock Mass

3.2.1. Strain Field Evolution. Strain is a property representative of material deformation. The strain of a specimen surface reflects the blasting intensity. The strain evolution of specimen surfaces under the explosion loading was investigated using DIC techniques to observe the effects of the blasting on the retained part. In Figure 6, the area in the yellow dotted box (808×343 pixels) is the calculated part. The left and right sides of the blasthole comprise the damaged rock mass (region A) and retained part (region B), respectively. The strain field of specimens (G1, G2, and G3) was calculated according to the method described in Section 2.3 and shown in Figure 11.

From Figure 12, it can be seen that after detonation, the stress wave propagated inside the specimen until reaching

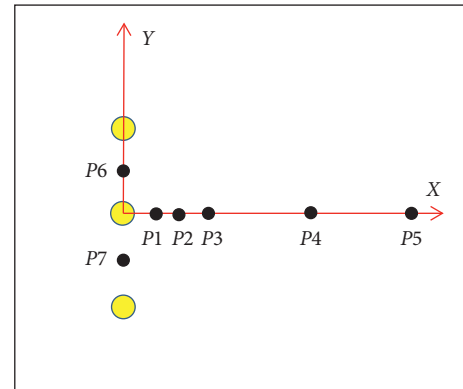


FIGURE 11: Monitoring points.

the surface. The strain concentration emerged first around the blasthole. For ease of description, the blastholes are numbered 1, 2, and 3 from top to bottom, as shown in Figure 6. For specimens G1 and G3, the strain concentration zone first appeared at the periphery of the blastholes 1 and 2 and the concentration zone range was small. Over time, the strain concentration zone gradually coalesced between blasthole 1 and blasthole 2 and the strain field around the

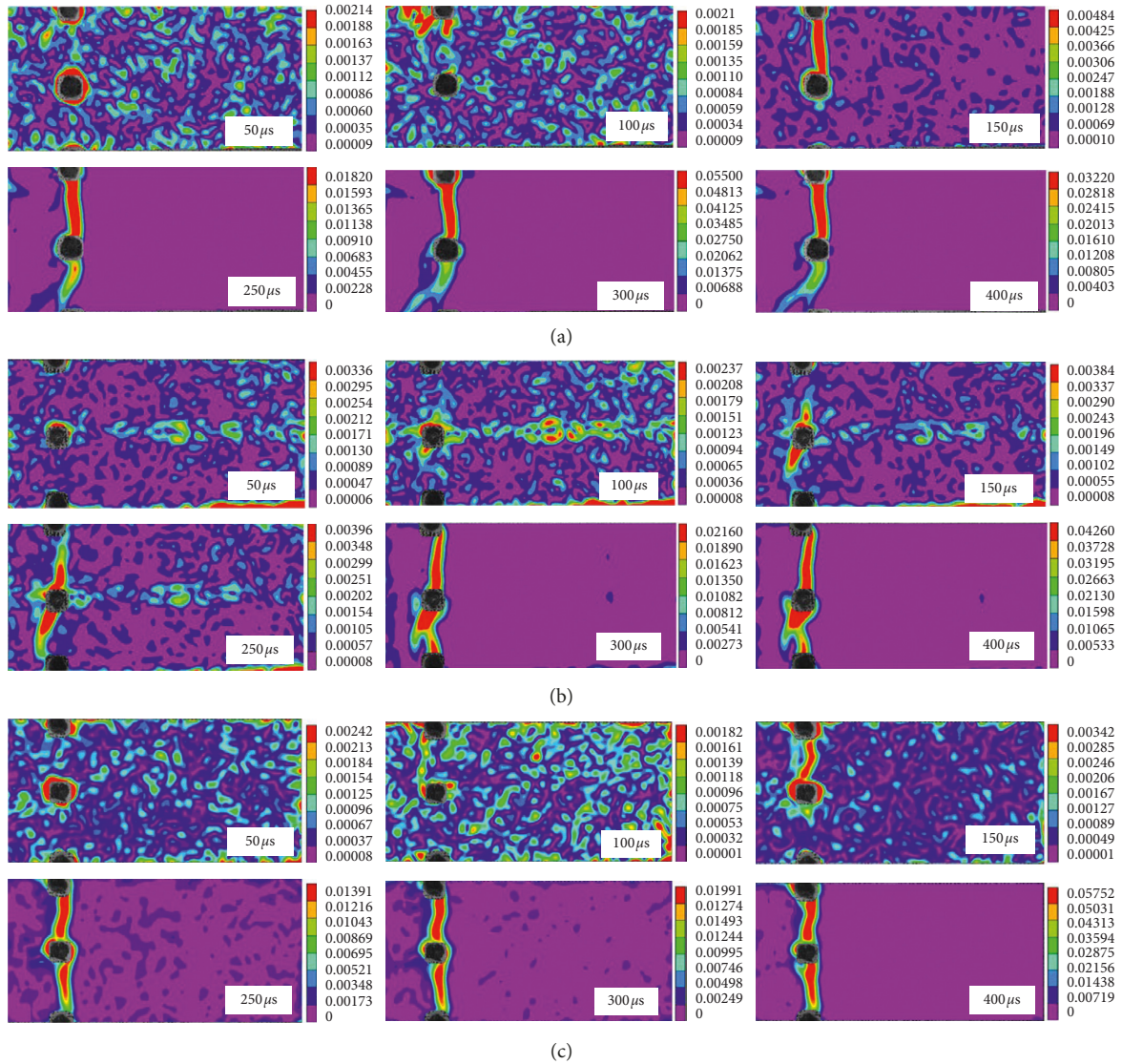


FIGURE 12: Strain field evolution of different specimens. (a) Strain field evolution of G1. (b) Strain field evolution of G2. (c) Strain field evolution of G3.

blasthole was chaotic. The crack continued to expand from blasthole 2 to blasthole 3, and the strain field around the blasthole gradually became stable. When the confining pressure was 1 MPa (G2), the strain concentration zone initially appeared around blasthole 2 and the crack expanded from blasthole 2 to blastholes 1 and 3 simultaneously.

Two forms of crack propagation modes were discovered in this experiment. Firstly, a crack between the two blastholes preferentially penetrated and then extended to the third blasthole, likely due to insufficient precision of the detonation time difference. Secondly, the crack is simultaneously expanded from the middle blasthole to the other two blastholes at the same time.

3.2.2. Peak Strain and Equivalent Strain Rate Attenuation of Retained Body. According to blasting theory, the blast-induced stress wave pressure is proportional to the specific

distance R ($R = r/r_{\text{hole}}$, where r is the distance from the calculation point to the center of the blasthole and r_{hole} is the blasthole radius) and decreases rapidly as distance increases. The unit *Inspector* was used to monitor and extract the strain signal on the surface of the specimen. An orthogonal coordinate was established for convenient analysis, and the center of blasthole 2 was chosen as the origin of the coordinate, the layout direction of the blasthole as the Y-axis, and the perpendicular direction as the X-axis, as shown in Figure 11. In this study, five monitoring points $P1$ (10 mm, 0 mm), $P2$ (15 mm, 0 mm), $P3$ (25 mm, 0 mm), $P4$ (75 mm, 0 mm), and $P5$ (125 mm, 0 mm) were chosen.

The strains at five monitoring points were extracted, denoised, and smoothed to obtain their respective strain-time curves. The strain at $P4$ and $P5$ hardly changes during the whole loading process. Therefore, only the points $P1$, $P2$, and $P3$ are described here (Figure 13). Under the three different conditions, the explosive stress waves propagated

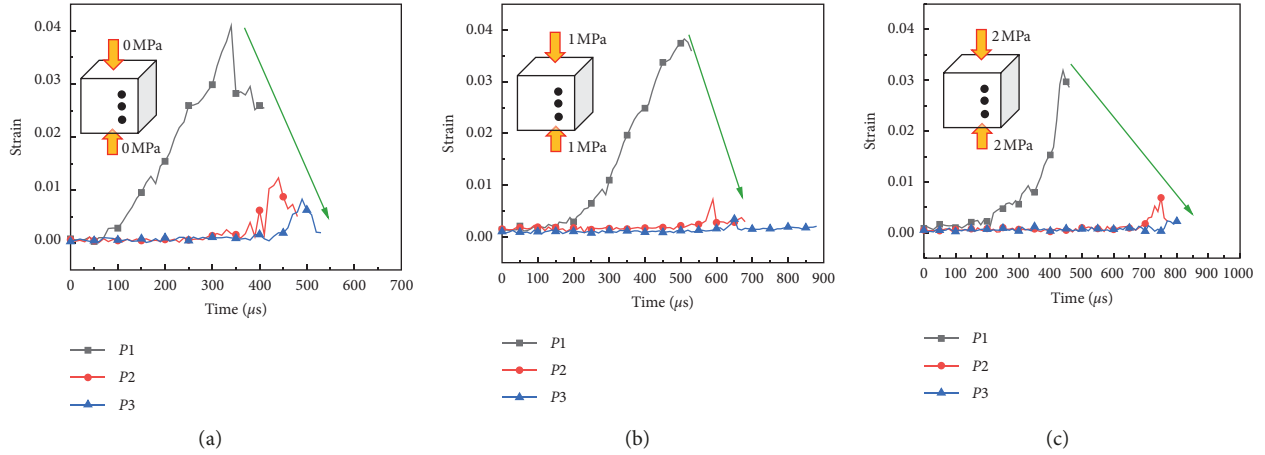


FIGURE 13: Strain history curves at different points of specimens.

to point $P1$ at 50, 100, and $100\ \mu\text{s}$, respectively, and rose to peak values at 400, 450, and $450\ \mu\text{s}$, respectively. Subsequently, due to the destruction of the rock mass around the blasthole, $P1$ point did not provide any further data. Points $P2$ and $P3$ are far from the blasthole, where the speckle was undamaged and more data could be obtained. The deformation greatly attenuated when the stress wave reached $P2$, and the peak strain attenuation amplitudes are 73.2%, 81.2%, and 78.7% compared to the value at $P1$, respectively. The peak strain at Point $P3$ in specimens G1, G2, and G3 continuously dropped down.

The equivalent strain rate reflects the deformation rate of the material and is an important representation of the material's dynamic response. The corresponding variability thus has crucial significance. The time at which the blast stress wave reaches the observation point is denoted here as t_0 and the corresponding strain as ε_0 . The time at which the strain reaches the peak value of $P1$ is defined as t , the peak strain is denoted as ε , and the equivalent strain rate is deduced by $\dot{\varepsilon} = (\varepsilon - \varepsilon_0)/(t - t_0)$. The peak strain and equivalent strain rates are listed in Table 3.

The curves of peak strain and the equivalent strain rate with respect to time of the observation point are demonstrated in Figure 14. When the confining pressure was 0 MPa, the peak strain decreased from $4.59e-2$ at point $P1$ to $8.31e-3$ at point $P3$ and the attenuation amplitude was 81.9%. The confining pressure was 1 or 2 MPa from point $P1$ to point $P3$; the attenuation value of peak strain was 92.1% and 92.8%, respectively.

For point $P1$, when the confining pressure changed from a nonconfined state (0 MPa) to a confining pressure constraint (1 MPa), the equivalent strain rate decreased from $191e-6\ \text{s}^{-1}$ to $67.14e-6\ \text{s}^{-1}$. This reflects the effect of confining pressure on the material deformation. The equivalent strain rate of points $P2$ and $P3$ showed a similar tendency with respect to point $P1$. We also found that when the confining pressure was 1 or 2 MPa, the equivalent strain rates of $P2$ and $P3$ were nearly equal. This suggests that the material equivalent strain rate is not sensitive to the confining pressure within a certain range.

The following conclusions can be drawn based on the above analysis. (1) The peak strain has an obvious attenuation with increasing distance. (2) When the observation point is close to the blasthole (10 mm), the peak value of the strain decreases as confining pressure increases. (3) When the observation point is far away from the blasthole (15 mm and 20 mm), the peak strain also decreases due to the effect of confining pressure. Under confining pressures of 1 MPa and 2 MPa, however, the peak strain is nearly unchanged. (4) Equivalent strain rate decreases as confining pressure increases, but the equivalent strain rate values are nearly consistent when the confining pressure is 1 MPa or 2 MPa.

3.3. Peak Strain Evolution between Blastholes. The strain-time curve between the blastholes indirectly reflects the inter-blasthole crack profile mode, so it is necessary to determine the strain evolution between the blastholes. Using the coordinate system established in Section 3.2.2, the curves of strain at measurement points $P6$ (0 mm, 20 mm) and $P7$ (0 mm, -20 mm) were extracted as shown in Figure 15.

When confining pressure was 0 MPa, the peak value of the $P6$ point strain was 0.10721 and the peak value of $P7$ point strain was 0.032. Their average value is 0.070, and the difference is 0.075. When the confining pressure was 1 MPa, the peak strains at points $P6$ and $P7$ were 0.095 and 0.057, respectively; the average and difference between them are 0.076 and 0.037, respectively. When the confining pressure increased to 2 MPa, the peak strains at points $P6$ and $P7$ were 0.116 and 0.113, respectively. The average value of $P6$ and $P7$ is 0.115, and the difference is 0.003. Overall, as confining pressure increased, the average value of the peak strain between the blastholes of the specimen gradually increased and the difference gradually decreased.

It can be concluded that confining pressure markedly influenced the strain evolution between blastholes $P6$ and $P7$. As the confining pressure increased, the strain difference between $P6$ and $P7$ decreased and the crack profile gradually changed from irregular zigzag to straight. The peak strain of the material between the blastholes also increased with confining pressure, indicating that the

TABLE 3: Peak strain and equivalent strain rate at each observation point.

Confining pressure (MPa)	Peak strain ϵ			Equivalent strain rate $\dot{\epsilon}$ (s^{-1})		
	P1	P2	P3	P1	P2	P3
0	$4.59E-02$	$1.23E-02$	$8.31E-03$	$191e-6$	$105e-6$	$67.14e-6$
1	$3.82E-02$	$7.20E-03$	$3.00E-03$	$126e-6$	$55.1e-6$	$17.6e-6$
2	$3.19E-02$	$6.80E-03$	$2.30E-03$	$120e-6$	$51.7e-6$	$13.1e-6$

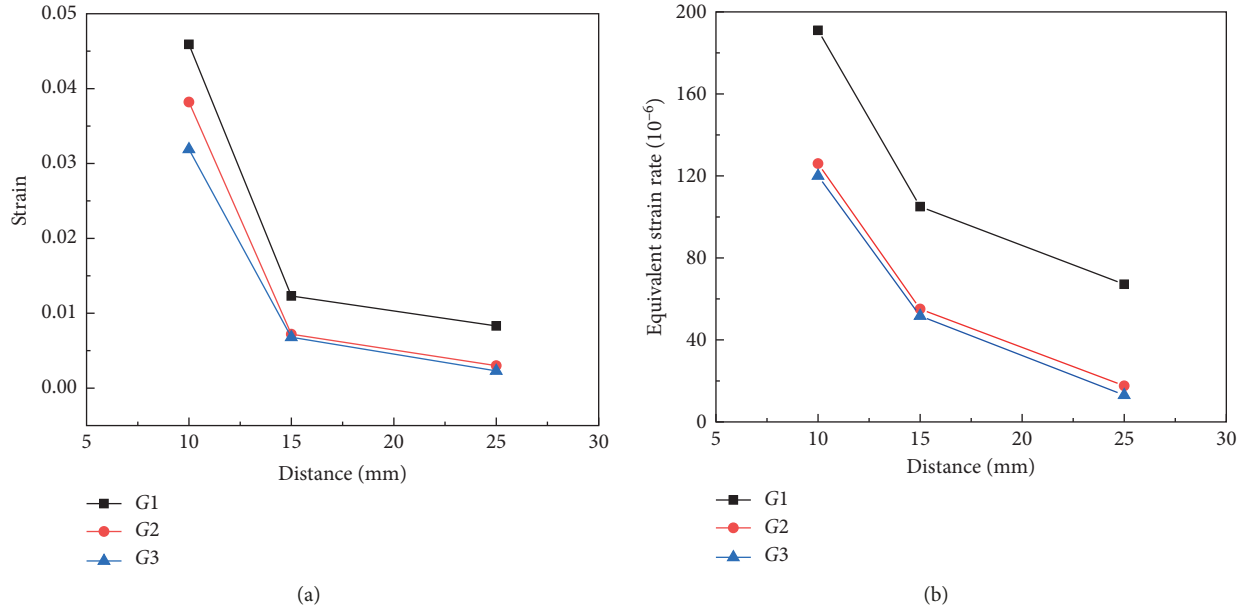


FIGURE 14: Variation of (a) peak strain and (b) equivalent strain rate with time.

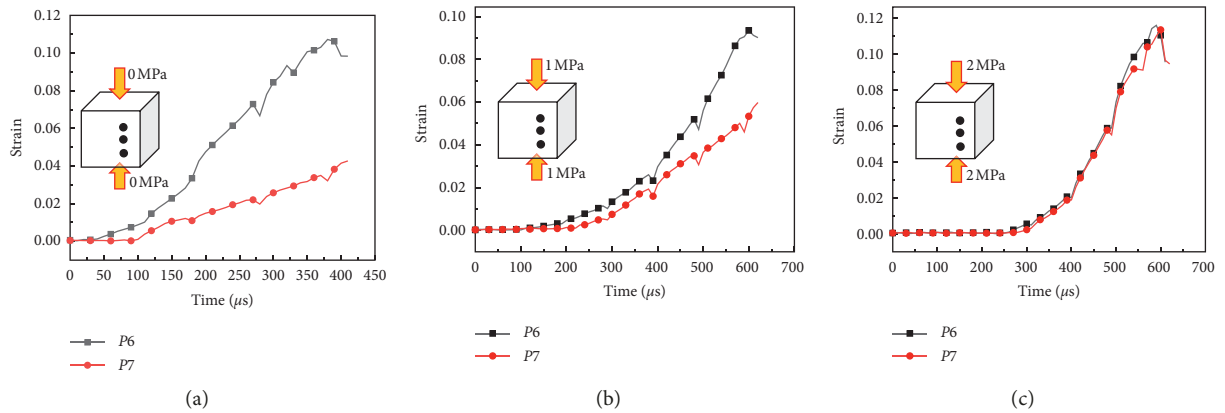


FIGURE 15: P6 and P7 strain curves with respect to time.

existence of confining pressure plays a guiding role in the release of blasting energy.

3.4. Damage Distribution of Surrounding Rock after Smooth Blasting. The damage degree D is an important index characterizing the damage to the surrounding rock mass. According to continuous damage mechanics, the damage degree D can thus be described by the changes in rock

density, elastic modulus, P-wave velocity and yield stress, and other factors [27]. The range of the D value is $\{0, 1\}$. When $D=0$, the surrounding rock mass can be considered to be in an ideal nondamaged state. At $D=1$, it can be assumed that the rock mass is completely broken. In this study, the initial damage of the specimen was ignored and only the damage of the specimen by blasting is considered. The damage calculation formula using the P-wave velocity method is shown as follows:

$$\begin{cases} E = V^2 \rho \frac{(1 + \mu_d)(1 - 2\mu_d)}{(1 - \mu_d)}, \\ D = 1 - \frac{E}{E_0} = 1 - \left(\frac{V}{V_0}\right)^2, \end{cases} \quad (4)$$

where E_0 is the elastic modulus of the gypsum before blasting, E is the specimen elastic modulus after blasting, V_0 and V are the P-wave velocity of the gypsum before and after blasting, respectively, μ_d is Poisson's ratio of the gypsum, and ρ is the density of the gypsum. The layout of the measuring points is shown in Figure 16, where the monitoring point distance from the blasthole is 25, 75, or 125 mm. The P-wave velocity data of the three monitoring points before and after blasting and the damage degree results calculated according to equation (4) are listed in Table 4.

As shown in Figure 17, the presence of confining pressure significantly affects the degree of damage. At the same monitoring point, a larger confining pressure resulted in less damage. When the confining pressure was equal, the damage value D gradually decreased as distance between the monitoring point and the blasthole increased. The slope of the curve becomes gentler as confining pressure increases; this again suggests that an increase in confining pressure can inhibit the damage to the surrounding rock under blast loading.

4. Discussion

According to the test results provided above, the presence of confining pressure is conducive to the formation of the roadway contour after smooth blasting and can inhibit damage to the surrounding rock. We will attempt here to explain this phenomenon as it relates to the explosion stress wave and in situ stress.

4.1. Explosive Stress Wave Effect. Figure 18 shows the crack propagation mechanism after single hole blasting. An explosive stress wave is generated after the explosive detonates which acts on the blasthole wall to produce a crushing zone. The crushing zone not only consumes a large amount of energy but also deteriorates the propagation medium of the subsequent stress wave resulting in a sharp attenuation of the wave. A portion of the stress wave continues to propagate forward, but its working capacity is reduced. The extent of damage to the rock mass decreases, and only tiny cracks are generated. As the stress wave attenuates continuously, the rock only generates elastic vibration. The stress wave is called an "elastic vibration wave" at this time.

A large amount of high-temperature and high-pressure gas, "detonation gas," is simultaneously generated after the explosive detonates. Unlike the explosive stress wave, the detonation gas propagates slowly at low intensity over a long duration. The detonation gas propagates around the blasthole, is wedged into the rock microcracks generated by the explosion stress wave, and produces an "air wedge" effect which causes the crack to further expand. The rock's fracture

toughness varies due to its anisotropy. Under the quasistatic action of the detonation gas, cracks preferentially expand along the weaker parts of the rock until forming several macroscopic main cracks. Unlike the transient stress wave, the detonation gas is actively regulated; the active adjustment process markedly affects crack propagation in the rock mass.

There are multiple blasthole interactions which occur in a smooth blasting scenario. For simplicity, we discuss here only the interaction of an explosion stress wave and a crack between two blastholes (Figure 19). After the explosion, the explosion stress wave behaves similarly to the single hole blasting scenario before reaching the crack generated by the adjacent blasthole. The P-wave of the explosion stress wave reaches the crack tip before the S-wave due to its greater velocity and has a certain inhibitory effect on the crack propagation. The subsequent S-wave interaction with the crack promotes the propagation of cracks along the blasthole line [28–30]. The existing crack in the direction of the blastholes further promotes other cracks to propagate in this direction while cracks in the other direction are slowed down and truncated due to transfer of the explosive gas. It is worth emphasizing that the propagation velocity of the stress wave is much greater than that of the crack and that the distance D between adjacent blastholes is short. Therefore, cracks are relatively underdeveloped in the blasthole wall before the stress wave acts on them; this is why the number of wing cracks around the a single blasthole after blasting is greater (and the cracks are longer) than after double hole blasting, as shown in Figure 20.

4.2. Effect of In Situ Stress on Crack Propagation. The existence of ground stress influences the stress field around the blasthole and the stress state of the rock mass. According to literature [19], under unidirectional stress, the radial normal stress and shear stress values at the circular hole are both zero; the circumferential normal stress can be expressed as follows:

$$\begin{cases} \sigma_\varphi = q_v (1 + 2 \cos 2\varphi), \\ \sigma_\rho = \tau_{\rho\varphi} = 0, \end{cases} \quad (5)$$

where q_v is the initial vertical stress and σ_φ , σ_ρ , and $\tau_{\rho\varphi}$ are the tangential stress, radial stress, and shear stress, respectively. When φ is 0° or 180° , the stress at the orifice is compressive. When φ is 90° or 270° , the orifice has the tensile stress at an absolute value equal to the compressive stress value, as shown in Figure 21(a). In the direction perpendicular to the vertical stress, the rock is in a state of compressive stress. In the direction parallel to the vertical stress, a tensile stress field lies near the orifice of the blasthole. Tensile stress results in favor of the initiation and propagation of cracks in the rock mass. The far region is the compressive stress field.

The rock is under the action of the superimposed explosion stress field and the in situ stress field after the explosive is detonated (Figure 21). As shown in Figure 22, in the direction perpendicular to the vertical stress, the

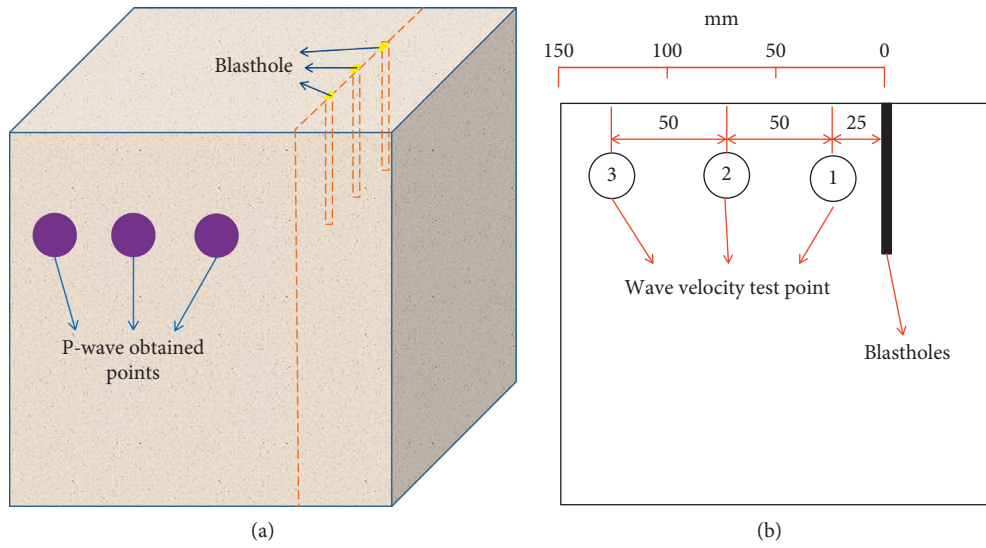


FIGURE 16: P-wave velocity acquisition position. (a) Global view. (b) Side view.

TABLE 4: P-wave velocity and damage value of each specimen.

Type of specimen	Monitoring point	Average P-wave velocity before explosion V_0 (m/s)	P-wave velocity after explosion V (m/s)	Damage D (%)
G1	1		1391	5.2
	2	1430	1411	2.6
	3		1421	1.2
G2	1		1442	3.9
	2	1471	1452	2.5
	3		1463	1.1
G3	1		1657	2.9
	2	1681	1666	1.7
	3		1670	1.2

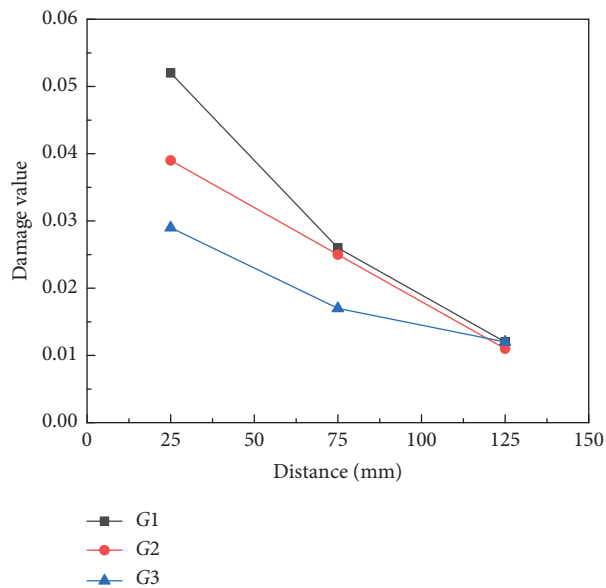


FIGURE 17: Damage value of different specimen measurement points after blasting.

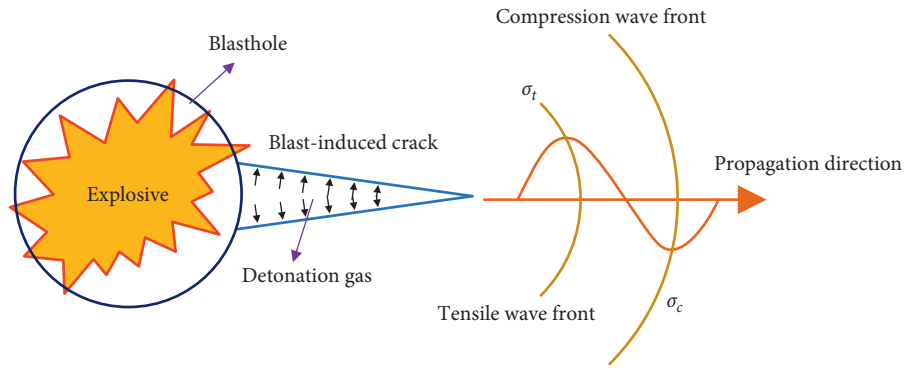


FIGURE 18: Mechanism of crack propagation after single hole blasting.

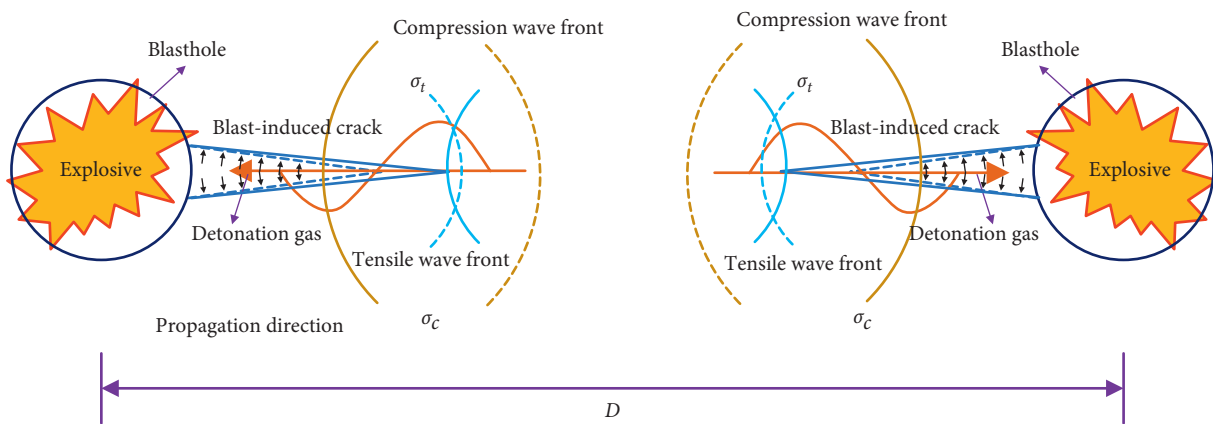


FIGURE 19: Mechanism of crack propagation after blasting of adjacent blastholes.

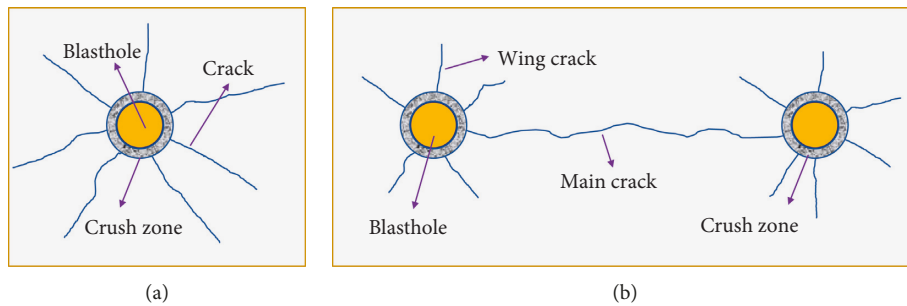


FIGURE 20: Crack distribution after (a) single hole and (b) double hole blasting.

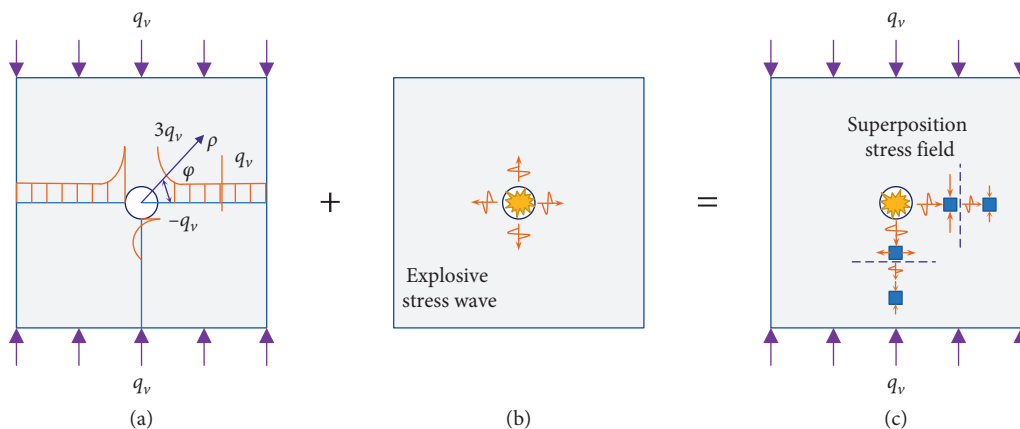


FIGURE 21: Schematic diagram of superimposed stress field.

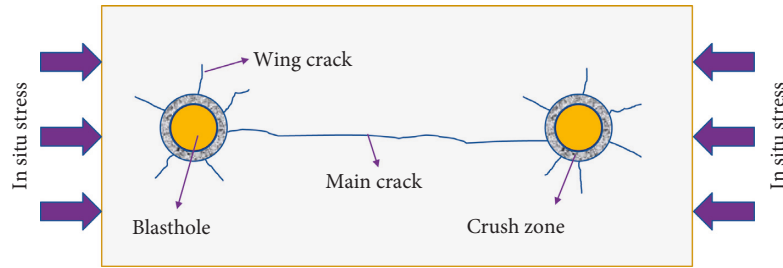


FIGURE 22: Schematic diagram of cracks distribution after blasting under compressive stress.

compressive stress field restrains and decelerates crack propagation as local microcracks appear [31]. The crack propagation will be promoted in vertical direction and the length of cracks increases [16].

Meanwhile, in the retained rock mass, vibration damping increases rapidly under increasing confining pressure and stress propagation process consumes more energy than the specimen without confining pressure. The strain and strain rate decrease as well, reflecting a reduction in damage to the surrounding rock.

The test method used in this study also has shortcomings, which may be remedied by further research. For example, gypsum with uniform, isotropic, and homogeneous characteristics was used as the test material; the anisotropy and nonuniformity of the rock mass were ignored, which should be considered in the future, and the effect of reflected stress wave on the rock damage is not considered [32]. Additionally, the explosive charge we used in the test is a uniform self-made charge and the charging parameters, detonation time, and detonation conditions were kept uniform. Other test conditions such as coupling coefficient, detonating time difference, and positive detonation were not considered. The impact of these factors on smooth blasting remains to be seen. In the future, we plan to explore this further.

5. Conclusion

This paper mainly discussed the fracture mode, strain evolution, and damage degree of retained rock masses after smooth blasting under various ground stresses. The main conclusions can be summarized as follows:

- (1) The crack profile after blasting shows that as the surrounding rock pressure increases, the crack profile between the blastholes gradually transitions from irregular zigzag to smooth and flat. The presence of confining pressure makes the crack outline more regular. The strain evolution between the holes suggests that crack formation effects are improved as the strain difference between the blastholes decreases.
- (2) The strain evolution curves of the retained body indicated that peak strain decreases obviously with increased distance. The existence of confining pressure also appears to have a certain influence on strain attenuation. The peak strain value decreases as

confining pressure increases, and the peak strain in the far field is not sensitive to confining pressure within the scope of this study. Equivalent strain rate evolution behaves similarly. The acoustic damage test revealed that the damage value D gradually decreases as the distance between the monitoring point and the blasthole increases.

- (3) Based on the strain evolution and damage distribution, confining pressure is largely responsible for the release direction of blasting energy. An increase in rock particle vibration damping also effectively prevents the growth in the strain and thus protects the surrounding rock from damage.

Despite some shortcomings, the conclusions presented in this paper also can provide workable guidelines for related engineering applications.

Data Availability

The data used to support the findings of this study are included within the article.

Conflicts of Interest

The authors declare no conflicts of interest.

Acknowledgments

This research was supported by the National Key Research and Development Program of China (no. 2016YFC0600903), the National Natural Science Foundation of China (no. 51774287), and the Fundamental Research Funds for the Central Universities (no. 2017QL05).

References

- [1] N. Yugo and W. Shin, "Analysis of blasting damage in adjacent mining excavations," *Journal of Rock Mechanics and Geotechnical Engineering*, vol. 7, no. 3, pp. 282–290, 2015.
- [2] H. B. Li, X. Xia, J. Li et al., "Rock damage control in bedrock blasting excavation for a nuclear power plant," *International Journal of Rock Mechanics and Mining Sciences*, vol. 48, no. 2, pp. 210–218, 2011.
- [3] M. Ramulu, A. K. Chakraborty, and T. G. Sitharam, "Damage assessment of basaltic rock mass due to repeated blasting in a railway tunnelling project—a case study," *Tunnelling and Underground Space Technology*, vol. 24, no. 2, pp. 208–221, 2009.

- [4] H. K. Verma, N. K. Samadhiya, M. Singh, R. K. Goel, and P. K. Singh, "Blast induced rock mass damage around tunnels," *Tunnelling and Underground Space Technology*, vol. 71, pp. 149–158, 2018.
- [5] J. B. Martino and N. A. Chandler, "Excavation-induced damage studies at the underground research laboratory," *International Journal of Rock Mechanics and Mining Sciences*, vol. 41, no. 8, pp. 1413–1426, 2004.
- [6] J. H. Yang, C. Yao, Q. H. Jiang, W. B. Lu, and S. H. Jiang, "2D numerical analysis of rock damage induced by dynamic in-situ stress redistribution and blast loading in underground blasting excavation," *Tunnelling and Underground Space Technology*, vol. 70, pp. 221–232, 2017.
- [7] Y. Hu, W. Lu, M. Chen, P. Yan, and J. Yang, "Comparison of blast-induced damage between presplit and smooth blasting of high rock slope," *Rock Mechanics and Rock Engineering*, vol. 47, no. 4, pp. 1307–1320, 2014.
- [8] L. X. Xie, W. B. Lu, Q. B. Zhang, Q. H. Jiang, G. H. Wang, and J. Zhao, "Damage evolution mechanisms of rock in deep tunnels induced by cut blasting," *Tunnelling and Underground Space Technology*, vol. 58, pp. 257–270, 2016.
- [9] X. Qiu, X. Shi, Y. Gou, J. Zhou, H. Chen, and X. Huo, "Short-delay blasting with single free surface: results of experimental tests," *Tunnelling and Underground Space Technology*, vol. 74, pp. 119–130, 2018.
- [10] H. K. Kutter and C. Fairhurst, "On the fracture process in blasting," *International Journal of Rock Mechanics and Mining Sciences & Geomechanics Abstracts*, vol. 8, no. 3, pp. 181–202, 1971.
- [11] H. P. Rossmanith, R. E. Knasmillner, A. Daehnke et al., "Wave propagation, damage evolution, and dynamic fracture extension—part II. blasting," *Materials Science*, vol. 32, no. 4, pp. 23–30, 1996.
- [12] D. Liu, W. Wang, L. Yang et al., "Holophotoelasticity study on mechanism of blasting under initiative stress field," *Journal of China Coal Society*, vol. 24, no. 6, pp. 612–614, 1999.
- [13] Y. Liu and J. Xu, "Numerical simulation of explosion in rock mass underground stress field," *Rock and Soil Mechanics*, vol. 28, no. 11, pp. 2485–2488, 2007.
- [14] W. Lu, M. Chen, X. Geng, D. Shu, and C. Zhou, "A study of excavation sequence and contour blasting method for underground powerhouses of hydropower stations," *Tunnelling and Underground Space Technology*, vol. 29, pp. 31–39, 2012.
- [15] J. Dai, "The controlled contour blasting technique and its parameter determination for rock tunnel at depth," *Explosion and Shock Waves*, vol. 24, no. 6, pp. 493–498, 2004.
- [16] X. P. Li, J. H. Huang, Y. Luo et al., "A study of smooth wall blasting fracture mechanisms using the timing sequence control method," *International Journal of Rock Mechanics and Mining Sciences*, vol. 92, pp. 1–8, 2017.
- [17] J. Li and G. Ma, "Analysis of blast wave interaction with a rock joint," *Rock Mechanics and Rock Engineering*, vol. 43, no. 6, pp. 777–787, 2010.
- [18] J. Li, G. Ma, and X. Huang, "Analysis of wave propagation through a filled rock joint," *Rock Mechanics and Rock Engineering*, vol. 43, no. 6, pp. 789–798, 2010.
- [19] R. Yang, C. Ding, Y. Li, L. Yang, and Y. Zhao, "Crack propagation behavior in slit charge blasting under high static stress conditions," *International Journal of Rock Mechanics and Mining Sciences*, vol. 119, pp. 117–123, 2019.
- [20] M. Sutton, W. Wolters, W. Peters, W. Ranson, and S. McNeill, "Determination of displacements using an improved digital correlation method," *Image and Vision Computing*, vol. 1, no. 3, pp. 133–139, 1983.
- [21] S. R. McNeill, W. H. Peters, and M. A. Sutton, "Estimation of stress intensity factor by digital image correlation," *Engineering Fracture Mechanics*, vol. 28, no. 1, pp. 101–112, 1987.
- [22] G. Han, M. A. Sutton, and Y. J. Chao, "A study of stationary crack-tip deformation fields in thin sheets by computer vision," *Experimental Mechanics*, vol. 34, no. 2, pp. 125–140, 1994.
- [23] J. Park, S. Yoon, T.-H. Kwon, and K. Park, "Assessment of speckle-pattern quality in digital image correlation based on gray intensity and speckle morphology," *Optics and Lasers in Engineering*, vol. 91, pp. 62–72, 2017.
- [24] B. Pan, Z. Lu, and H. Xie, "Mean intensity gradient: an effective global parameter for quality assessment of the speckle patterns used in digital image correlation," *Optics and Lasers in Engineering*, vol. 48, no. 4, pp. 469–477, 2010.
- [25] R. Yang, C. Ding, L. Yang, and C. Chen, "Model experiment on dynamic behavior of jointed rock mass under blasting at high-stress conditions," *Tunnelling and Underground Space Technology*, vol. 74, pp. 145–152, 2018.
- [26] D. Xue, H. Zhou, W. Ren et al., "Multi-fractal characteristics of joint geometric distribution of granite in Beishan," *Rock and Soil Mechanics*, vol. 37, no. 10, pp. 2937–2944, 2016.
- [27] J. Lemaitre, *A Course on Damage Mechanics*, Springer, Berlin, Germany, 1992.
- [28] P. Qiu, Z. Yue, S. Zhang, and Z. Li, "An in situ simultaneous measurement system combining photoelasticity and caustics methods for blast-induced dynamic fracture," *Review of Scientific Instruments*, vol. 88, no. 11, p. 115113, 2017.
- [29] P. Qiu, Z. Yue, and R. Yang, "Mode I stress intensity factors measurements in PMMA by caustics method: a comparison between low and high loading rate conditions," *Polymer Testing*, vol. 76, pp. 273–285, 2019.
- [30] R. Yang, P. Xu, and C. Chen, "Interaction between blast stress waves and cracks," *Explosion and Shock Waves*, vol. 39, no. 8, pp. 30–40, 2019.
- [31] K. Xia, Y. Xu, W. Yao et al., "Experimental study of dynamic fracture behavior of brittle rockplate under static pre-loading," *Chinese Journal of Rock Mechanics and Engineering*, vol. 36, no. 5, pp. 1122–1132, 2017.
- [32] P. Qiu, Z. Yue, R. Yang, and J. C. Li, "Effects of vertical and horizontal reflected blast stress waves on running cracks by caustics method," *Engineering Fracture Mechanics*, vol. 212, pp. 164–179, 2019.



Hindawi

Submit your manuscripts at
www.hindawi.com

